Check for updates

Fracture surface formation of notched 2017A-T4 aluminium alloy under bending fatigue

Wojciech Macek

© The Author(s) 2021

Abstract The effect of cyclic loading on facture surface topology in notched components made by aluminium alloys is not completely clear. Fractography and fracture mechanics can help to understand this interdependency. This paper aims to study the distribution of the fracture surface roughness of notched 2017A-T4 aluminium alloy after bending fatigue using an optical focus-variation surface measurement technique by applying the fracture zone concept. The effects of stress level at the notch root and the load ratio on fatigue crack growth and fracture surfaces are analysed. Profile and areal surface parameters of four fracture surface regions were investigated at incremental crack lengths of the specimens. Studies have confirmed that the surface areas associated with the main stages of fatigue phenomenon (i.e. crack initiation, crack propagation, and final rupture) have significant differences in roughness which can be explained by the different loading scenarios. Overall, fatigue fracture surfaces have smallest roughness values at the crack initiation stage and a gradual increase during the fatigue crack growth stage.

W. Macek (✉)
Faculty of Mechanical Engineering and Ship Technology,
Gdańsk University of Technology, Gdańsk, Poland
e-mail: wojciech.macek@yahoo.com

1 Introduction

There are numerous methods to study the different mechanisms of fatigue phenomena, which are reflected in the increasing number of fatigue testing approaches for the most critical cases (McDowell 1989; Berto and Zappalorto 2011; Martins et al. 2020; Moreira et al. 2020; Mendes et al. 2020). The failure element on the fracture surface depends on the material type and the loading conditions under which it is subjected during its lifetime (Carpinteri et al. 2002; Faszynka et al. 2016; Branco et al. 2018; Correia et al. 2018; He et al. 2021). This loading history can be traced from the fracture surface topology using fractography concepts.

2017A-T4 is a typical aluminium alloy (Rozumek and Faszynka 2020) often used in structural elements containing notches and other stress concentrators. These geometrical details when subjected to cyclic loading are susceptible to fatigue crack initiation which can culminate in fatigue failure. Fracture mechanics and fractography are two branches of modern engineering currently used to investigate the mechanical behaviour of structural elements during and after fatigue failure, respectively (Zeravcic et al. 2006; Macek et al. 2017, 2020b, c, d; Branco et al. 2020; Kowal and Szala 2020). One of the methods of fracture-surface topography analysis is FRASTA, developed by SRI International (Kobayashi and Shockey 2010) and further improved by (Cao et al.

2014; Martelo et al. 2019). Another approach, called total fracture area method, was used by Macek to analyse the fracture topographies for various engineering materials and loading cases, including single bending, single torsion and their combinations (see, for example, the reference (Macek et al. 2020a, 2021)). This and other cited works present robust attempts to apply various fatigue fracture surface parameters (such as Rx profile parameters, areal Sx, volume Vx, as well as the fractal dimension Df) to explain the effect of various fatigue variables, namely loading type and specimen geometry. Crack lengths and the number of cycles to failure were also compared to the metrological parameters of fractured surfaces, showing a direct interdependence.

Furthermore, stress concentrators are usually weak points and may be potential locations for failure. However, the notch behaviour cannot be dissociated from the loading type and the loading level (Łagoda et al. 2001; Kulesa et al. 2016; Skibicki and Pejkowski 2017). There are several fracture mechanisms in the literature for describing the fracture process of notched specimens under bending loading (Owsiński and Niesłony 2016; Wu et al. 2018). In the literature, these fracture mechanisms were examined based on quantitative analysis of fracture surface morphology using fractographic parameters (Slámečka et al. 2010; Macek 2019a, b; Lauschmann et al. 2019). Evaluation of surface roughness for the specimen regions during testing were also studied previously (Wang et al. 2013). Optical surface profiling was useful in these cases (Kaplonek et al. 2016; Świrad et al. 2019).

In the literature, there are some attempts to correlate the surface roughness and volumetric defects with fatigue life. This has been investigated for axisymmetric complex surfaces (Aono and Noguchi 2005), for short cracks under mixed mode loading (Zhang and Fatemi 2010), or for fatigue crack growth at the subgrain scale (McDowell 1989). A smaller number of papers has tried to investigate the relationships between fatigue and fracture parameters and fracture surface roughness (Arakawa and Takahashi 1991; Slámečka et al. 2010; Kobayashi and Shockey 2010). Nevertheless, the correlation between fracture roughness parameters and fatigue properties for notched samples made of aluminium alloy has not been systematically investigated yet. Therefore, in this study, different fracture zones associated with the fatigue phenomenon will be first compared using areal

and profile parameters for notched specimens of 2017A-T4 aluminium alloy under fatigue loading. More specifically, this paper aims to investigate the effects of bending stress level and stress ratio on fatigue crack growth rates and then correlate the effects with the associated values of the fracture surface parameters measured on different locations of the fracture zones, i.e. different areas and profiles of fracture surfaces collected in the experiments.

2 Experimental procedure

2.1 Material

The chemical composition and the main monotonic properties of the tested material, a 2017A-T4 aluminium alloy, are given in Tables 1 and 2, respectively (Rozumek and Faszynka 2016). The microstructure of the material, examined from a metallographic microscope with different magnifications is exhibited in Fig. 1. As can be seen, it is characterised by banded grain arrangement in the direction of rolling direction.

2.2 Bending fatigue tests

The cyclic bending fatigue tests were carried out on a MZGS-100 fatigue machine (Rozumek and Faszynka 2020) to evaluate the fatigue crack growth rates. The tests were conducted under load-control mode, with the objective of controlling the applied bending, at a load frequency of 28.0 Hz. A portable microscope with a constant magnification of 25 × with a micrometer accuracy of $\Delta a = 0.01$ mm was used to measure the crack length during the tests while recording the associated number of loading cycles.

The specimen geometries, presented in Fig. 2, consisted of flat beams with a one-sided external V-notch. The notch geometry has an angle of 60° and a radius (ρ) of 0.2 mm. The tests were performed from crack initiation to total failure (i.e. separation of

Table 1 Monotonic quasi-static tension properties of the 2017A-T4

Material	σ_y, MPa	σ_{us}, MPa	E, GPa	ν (–)
2017A-T4	382	480	72	0.32

Table 2 Composition of a substance of the 2017A-T4 (wt%)

Material	Cu	Mn	Zn	Mg	Fe	Cr	Si	Ti	Al
2017A-T4	4.15	0.65	0.50	0.69	0.70	0.10	0.45	0.20	Bal
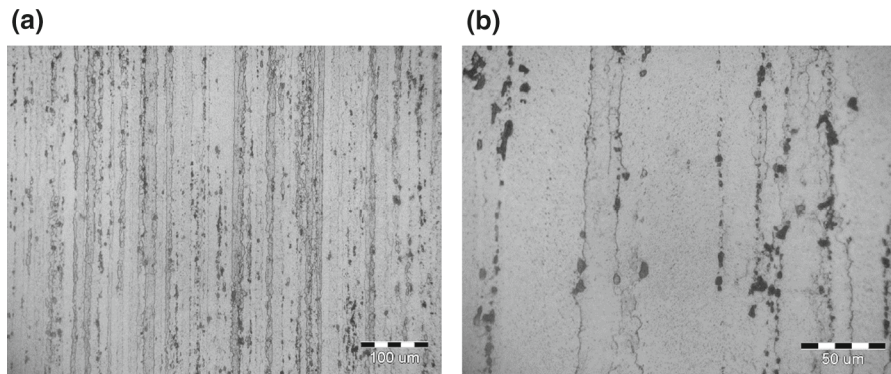
Fig. 1 Microstructure of the 2017A-T4 aluminium alloy at magnifications: **a** 200 ×, **b** 500 ×

Fig. 2 Geometry of tested beams (dimensions in millimetres)
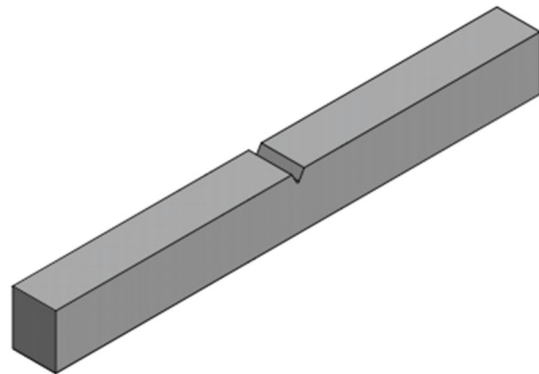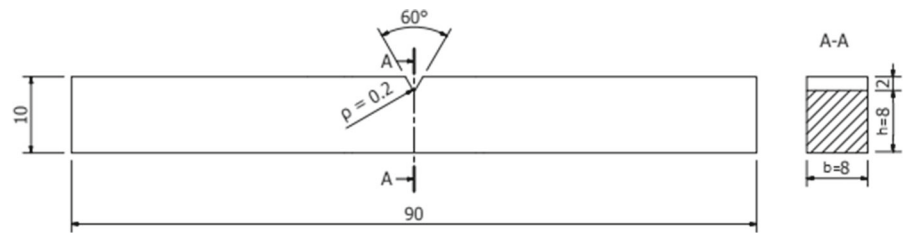
specimens into two pieces) and three stress ratios ($R = \sigma_{min}/\sigma_{max} = -1, -0.5$, and 0) and two maximum nominal normal stress amplitude ($\sigma_{a,max}$). Details about the loading cases and the numbers of cycles to failure, N_f, are summarized in Table 3. The specimens were numbered according to their fatigue durability. Samples S1 and S7 have the smallest and largest number of cycles to failure, respectively.

Maximum normal stress amplitude at the notch root, $\sigma_{a,max}$, can be defined using the following relationship:

Table 3 Loading scenarios of the tested specimens

Specimen	$\sigma_{a,max}$ (MPa)	R	N_f (cycles)
S1	698	0	$12 \cdot 10^3$
S2	349	0	$17 \cdot 10^3$
S3	698	-0.5	$20 \cdot 10^3$
S4	698	-1	$22 \cdot 10^3$
S5	698	-1	$24 \cdot 10^3$
S6	349	-0.5	$52 \cdot 10^3$
S7	349	-1	$322 \cdot 10^3$

$$\sigma_{a,max} = \sigma_a K_t \tag{1}$$

where σ_a is nominal normal stress applied and K_t is the theoretical notch factor. For $\rho = 0.2$ mm, K_t is equal to 3.76 (Rozumek and Faszynka 2017). The nominal stress amplitude (σ_a) was determined from the formula:

$$\sigma_a = \frac{6M_B}{bh^2} \tag{2}$$

where M_B is the bending moment, b is the width, and h is height of the cross-section (see Fig. 2).

2.3 Focus-variation fractography and 3D reconstruction

Morphologic measurements of the fracture surfaces were performed with an Alicona G4 optical profilometer using focus-variation technology with $\times 10$ magnification lens. Due to the restricted field of view, 10 rows and 7 columns were stitched together to map the entire fracture area. Each individual micrograph had a vertical resolution of 79.6 nm and a lateral resolution of 3.9 μm. The fracture surface maps were processed with MountainsMap software for quantitative analysis and visualisation. A similar configuration of equipment and software for surface analysis was used in the previous studies (Allum et al. 2020; Kahlin et al. 2020).

Four profiles (P1–P4) and four areas (A1–A4) were extracted from the measured surfaces in accordance with the direction of crack propagation. Figure 3 shows the locations of the studied profiles and areas on the fracture surface. The measured profiles were 2 mm long, and the areas were rectangles with an area of 1 mm × 0.5 mm. The paths P1–P4 and the areas A1–
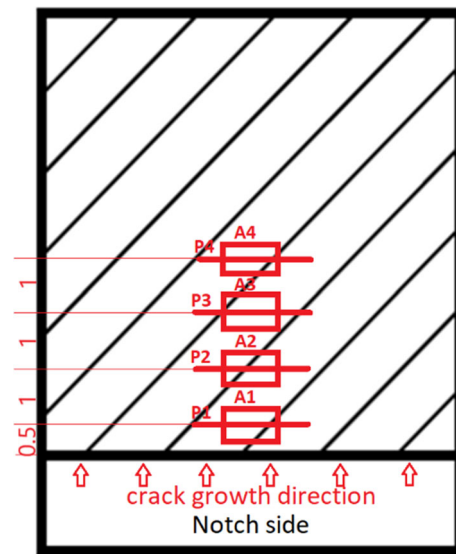
Fig. 3 Locations of the studied profiles and areas on the fracture

A4 were selected at the center of the fracture surface because crack symmetry was observed. In addition, the fatigue crack initiated from the notch centre and, therefore, the center axis is more representative.

Figure 4 presents the 3D views of specimen fractures S1 to S7 with the marked areas A1 to A4 (Fig. 4a–g) and the marked profiles P1 to P4 (Fig. 4a–g) in pseudo colour views. The scale represents the z-axis height of the individual fatigue fracture surface points. Overall, important differences in the colour gradients can be observed which can be associated with the different stress levels and applied stress ratios. We can see that the lower values are present near the notch region.

2.4 Crack growth description

Fatigue crack growth rates, determined as a function of the stress intensity factor range, were described using the Paris equation (Paris and Erdogan 1963):

$$\frac{da}{dN} = C(\Delta K_I)^m \tag{3}$$

where $\Delta K_I = K_{max} - K_{min}$ is stress intensity factor range, and C and m are material constants determined experimentally by using a best fitting technique. Stress intensity factor (SIF) range ΔK_I, may be written for bending as:
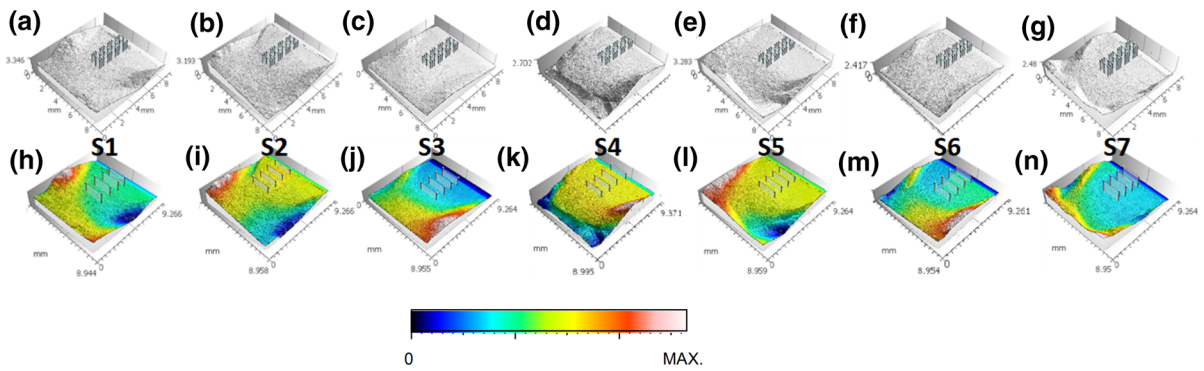
Fig. 4 3D views of the S1–S7 specimens with marked (**a–g**) areas A1–A4 (**h–n**) profiles P1–P4. Pseudo-colour views represent the z-axis coordinate in relation to the minimum point

$$\Delta K_I = Y_1 \Delta\sigma_n \sqrt{\pi(a + a_0)} \qquad (4)$$

where $\Delta\sigma_n$ is the nominal stress range for bending evaluated from the gross area, a_0 is the notch depth, a is crack length, and Y_1 is the correction factor dependent on the specimen geometry and loading type. The correction factor for bending was calculated from the following formula (Pickard 1986):

$$Y_1 = 5/\sqrt{20 - 13((a + a_0)/h) - 7((a + a_0)/h)^2} \qquad (5)$$

where h is the height of the specimen (see Fig. 2).

3 Results of the notched specimens

3.1 Experimental fatigue behaviour

Figure 5 represents the number of cycles to failure N_f obtained from notched specimens with different load ratios (Fig. 5a) and stress levels at the notch root (Fig. 5b). At the same stress amplitude, fatigue life decreases with the increase of stress ratio, due to the mean stress effect. For second figure (Fig. 5b), the increase in stress level reduces the fatigue lifetime.

The length of fatigue cracks was measured using a light microscope on both sides of the specimen. Over the cyclic fatigue bending tests, the cracks propagated in a symmetric manner along the both sides of the specimens. Fatigue cracks initiated from the notch tip. Figure 6 plots the crack length against the number of cycles obtained in the experiments for the specimens tested under cyclic bending loadings.
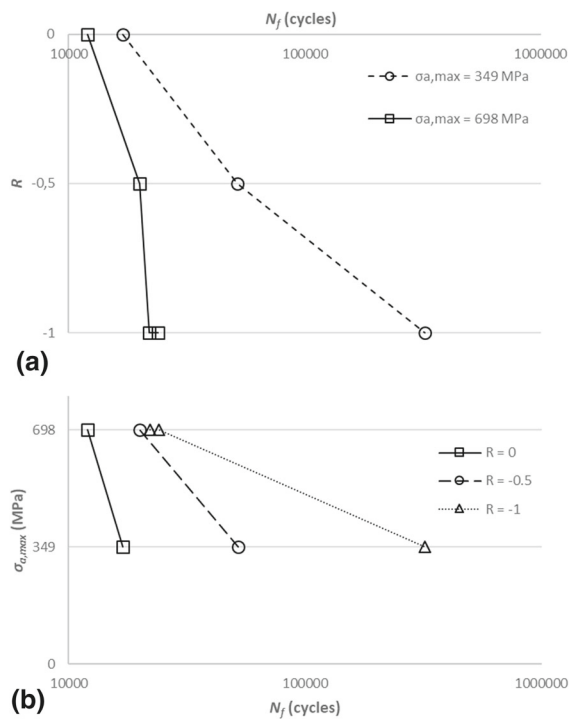

Fig. 5 Number of cycles to failure Nf of notched 2017A-T4 alloy specimens for **a** three different load ratios R, **b** two values of stress at the notch root $\sigma_{a,max}$

Briefly, the results shows that fatigue crack initiation and fatigue crack growth rates are faster for higher stress levels at the same stress ratio, and are faster for higher strain ratios at the same stress level. In the first case, it can be justified by the mean stress effect which increases with the stress ratio increase, while in the second case it can be explained by the higher crack driving force associated with higher stress levels.

Fig. 6 Fatigue crack length (a) versus numbers of loading cycles (N) under bending with profiles P1–P4 and areas A1–A4 marked on the cross section
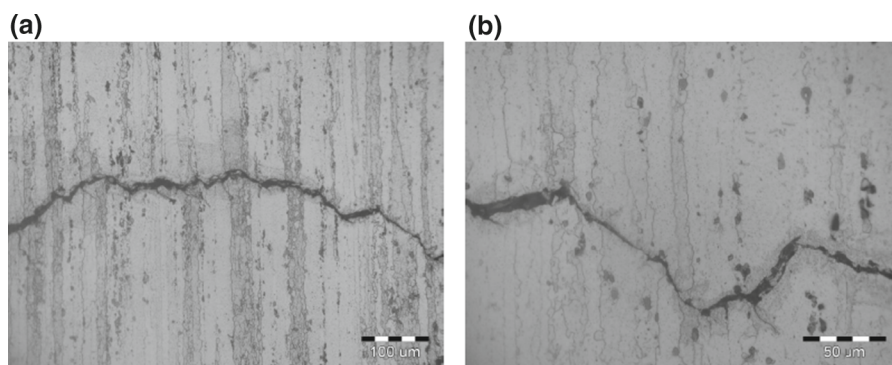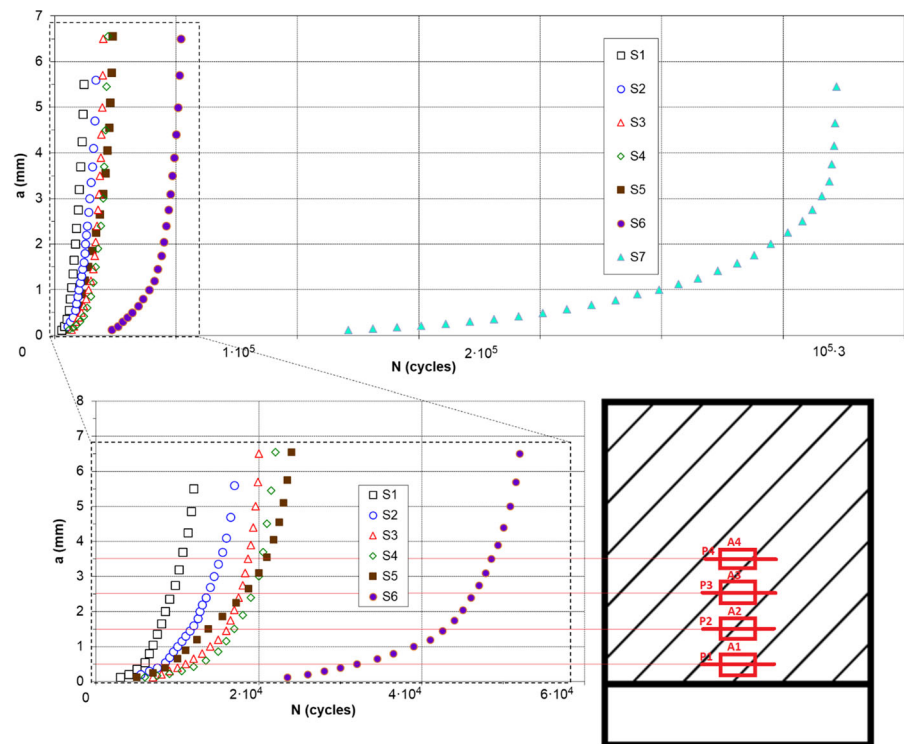

Fig. 7 Fatigue crack propagation in 2017A-T4 alloy (specimen S7) at magnification: **a** 200 ×, **b** 500 ×

Different magnifications were chosen to present the path of the main fracture about 0.7 mm long (Fig. 7a). Figure 7b shows the final course of a crack with a length of about 250 μm. The image was cut out from Fig. 7a and enlarged, in order to conduct detailed analysis of the crack development. Figure 7 shows the microstructure of the tested sample, where the durability of Nf = 322,000 cycles was observed. The main crack has a very irregular nature and runs transcrystalline through the grains of the solid solution α. In the 2017A-T4 alloy, numerous side cracks of various

lengths (from a dozen to about 100 μm) depart from the main crack. In many cases, they are generated at the grain boundaries of a solid solution.

3.2 Fracture surface measurement

Figure 8a displays the topographies and profiles (P1–P4) for all investigated fracture surfaces (S1–S7). In general, there is an increase in the size of the peaks and valleys with the crack length. Only in the case of the P1 profile we can see are large faults due to the stress
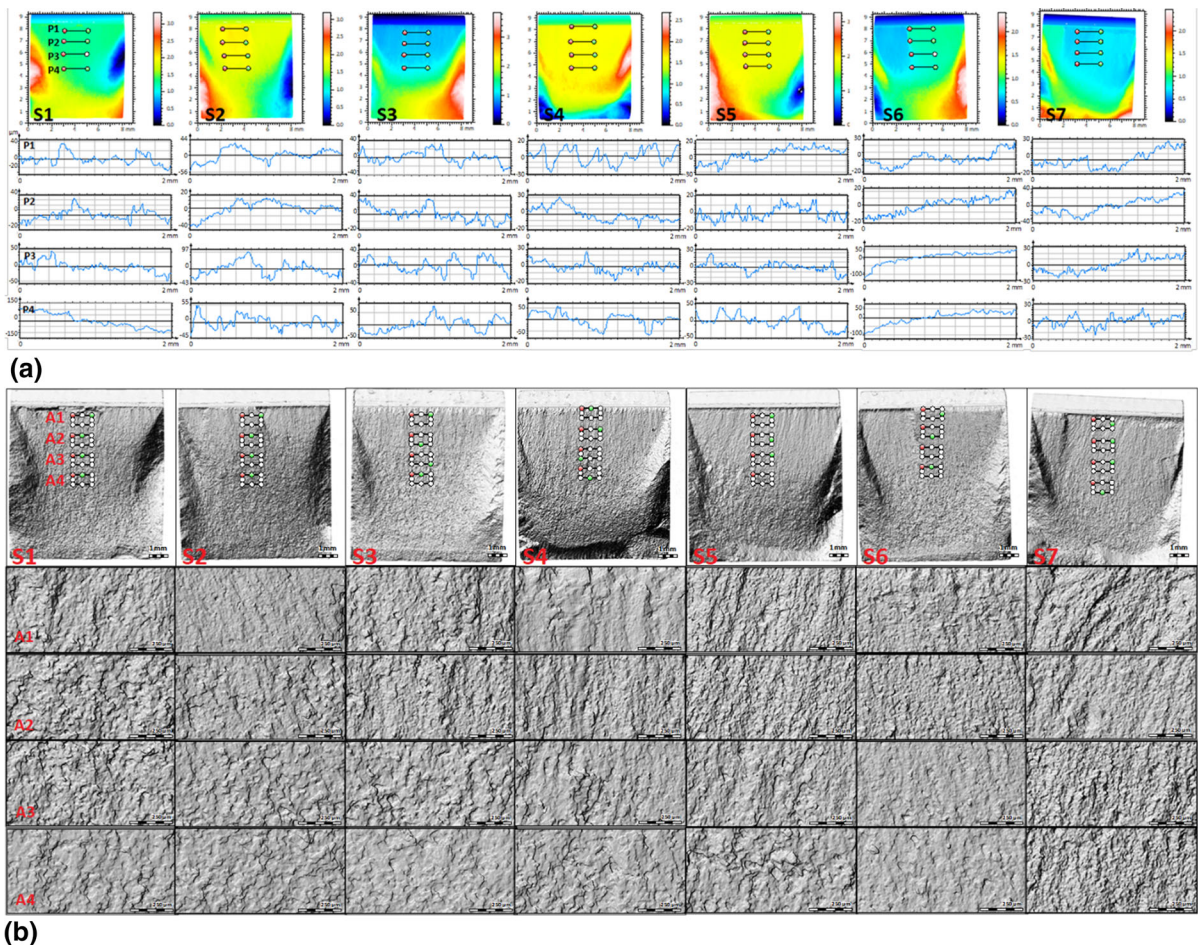
(a)

(b)

**Fig. 8 a** Profiles P1–P4 for specimens S1–S7, and **b** areas A1–A4 for specimens S1–S7

concentration effects at notch bottom. Regarding the surface zones (A1–A4) for the investigated specimen fractures, it can be distinguished that with the crack propagation, the surface of the fracture tends to be rougher.

Figure 9 represents all measurement results for Rx profiles parameters (Fig. 9a), Sx areal parameters (Fig. 9b), and Vx volume parameters (Fig. 9c). Table 4 defines the used parameters according to the ISO 4287 and ISO 25,178 standards.

3.3 Topography analysis of selected fracture areas

Figures 10 and 11 extend the topography analysis of selected areas of the measured fracture zones. Namely, Fig. 10a and 11a show stitching the original microscopic images made to realize three-dimensional measurements using the focus-variation technique.

Photo simulation (Figs. 10b, 11b) is a visualization in simulated picture mode and also allowing to choose the light settings, displays great image quality and high resolution, giving us a general view of the surface. *3D view of the surface* (see Figs. 10c and 11c) displayed the topography within interactive 3D visualization, while in *pseudo-colour view of the surface* (Fig. 10d and 11d) colours represents of heights on a measured area. *Furrows* study (Figs. 10e, 11e) calculate parameters with regard to the valleys network, as depth and density of furrows. These renderings are obtained through Fourier transform applied on topographic height profile functions that simulate furrows about peaks and valleys along the surface for better qualitative visualization of the material's texture. Whereas *slope distribution* (Fig. 10f, 11f) shows slope and orientation of all triangular tiles composing the fracture surface, and analyze their distribution, where
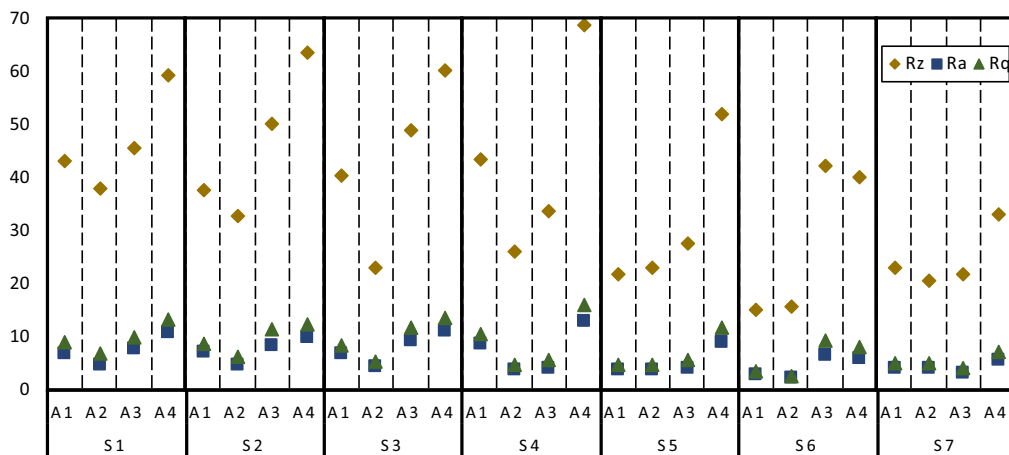
(a)
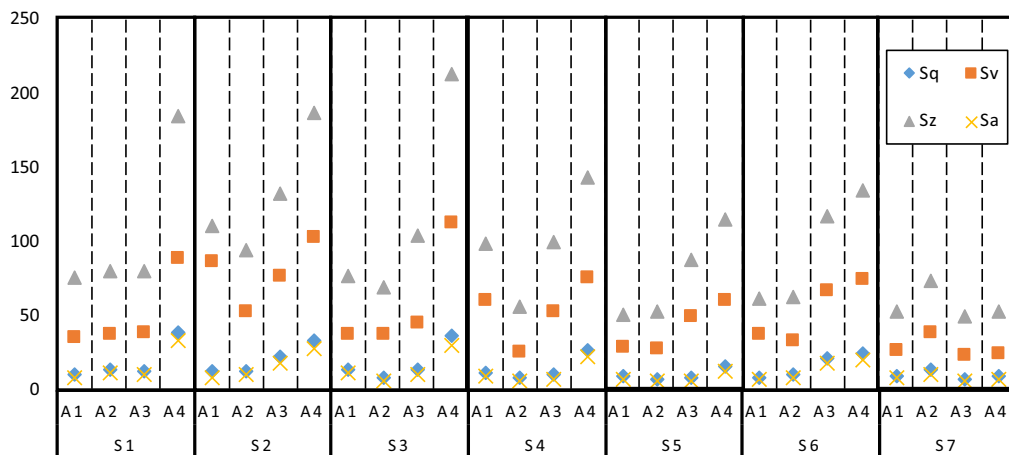
(b)
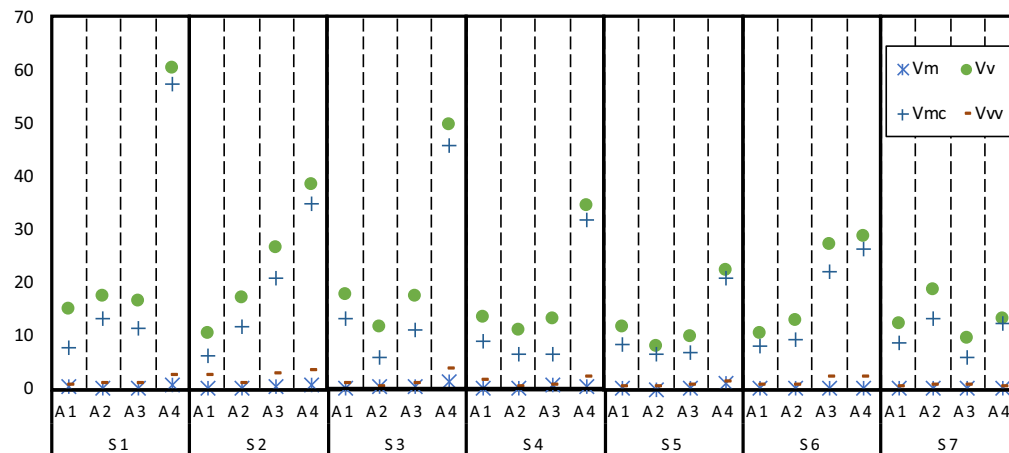
(c)

the normal vector of each tile is used as a reference for calculation. Also a useful function from the point of view of these studies is *converted into a series—profile curves* (Figs. 10g and 11g), which convert into a series of profiles, using the whole surface. The series of profiles plot also shows analyze of multiple profiles extracted from the same surface from a statistical point of view, namely the mean curve and the upper and lower envelope. The last parameter taken into account in this study is *peak count distribution* (Fig. 10h and 11h) showing the distribution of the peak heights.

The 2D and 3D topographic images showed different morphologies for the S7 A1 (see Fig. 10a–d) and S7 A4 (see Fig. 11a–d) surface sections. Observing the A1 and A4 surfaces for S7 specimen, it is noticed the difference in granularity and surface geometry of the fracture plane. In the A4 zone, larger differences in surface grain are visible, while in A1 it is noticed directionality, which is manifested by elongated grains. Figures 10e and 11e show contours between the furrows that give the representative structures of the A1 and A4, respectively. The A4 region is characterized by greater depth of furrows and

mean density of furrows. As for the slope distribution (see Fig. 10f and 11f), the mean angle of slope is 14.71° for the A1 area, while for it is 16.50° for the A4 area. Regarding the profile series plots, for A1 and A4, these are Figs. 10g and 11g, respectively. These figures show a much larger range of scattering of the profile values for the A4 area, which is related to the greater range of pits and valleys. However, when it comes to peak count distribution (see Figs. 10h and 11h), a greater maximum number of peaks per square millimeter occurs for A4 area (over 40), while for the A1 area, it is below 25. For both surfaces, the maximum peak values oscillate around 40 μm, but for the A1 area, they are more spread over the entire range (less than 20 μm to over 60 μm).

4 Discussion

Figure 12 shows the graphs of the fatigue crack growth rate (da/dN) as a function of the stress intensity factor range (ΔK_I) under bending loading described using the Paris equation (Eq. (3)). Analysis of the graphs in Fig. 12 shows that the change in the stress value from $\sigma_{max} = 349$ MPa to $\sigma_{max} = 698$ MPa significantly influences the increase in the fatigue crack growth rate for the tested R coefficients.

Table 4 Selected parameters for the fatigue fracture surface description according to ISO 4287 and ISO 25178

|			
Profile parameters (Rx), ISO 4287			
Rz	μm	Maximum height of the profile	
Ra	μm	Arithmetic mean deviation of the assessed profile	$Ra = \frac{1}{lr}\int_0^{lr}|z(x)|dx$
Rq	μm	Root mean square deviation of the assessed profile	
Height parameters (Sx), ISO 25178			
Sq	μm	Root-mean-square height	$Sq = \sqrt{\frac{1}{A}\iint_A z^2(x,y)dxdy}$
Sv	μm	Maximum pit height	Absolute value of the height of the largest pit within the defined area
Sz	μm	Maximum height	Height between the highest peak and the deepest valley
Sa	μm	Arithmetical mean height	$Sa = \frac{1}{A}\iint_A |z(x,y)|dxdy$
Functional parameters (volume) (Vx), ISO 25178			
Vm	mm³/mm²	Material volume	Parameters describing the characteristics of the volume
Vv	mm³/mm²	Void volume	of the appropriate size to the surface area of the surface
Vmc	mm³/mm²	Core material volume	being examined
Vvv	mm³/mm²	Pit void volume	
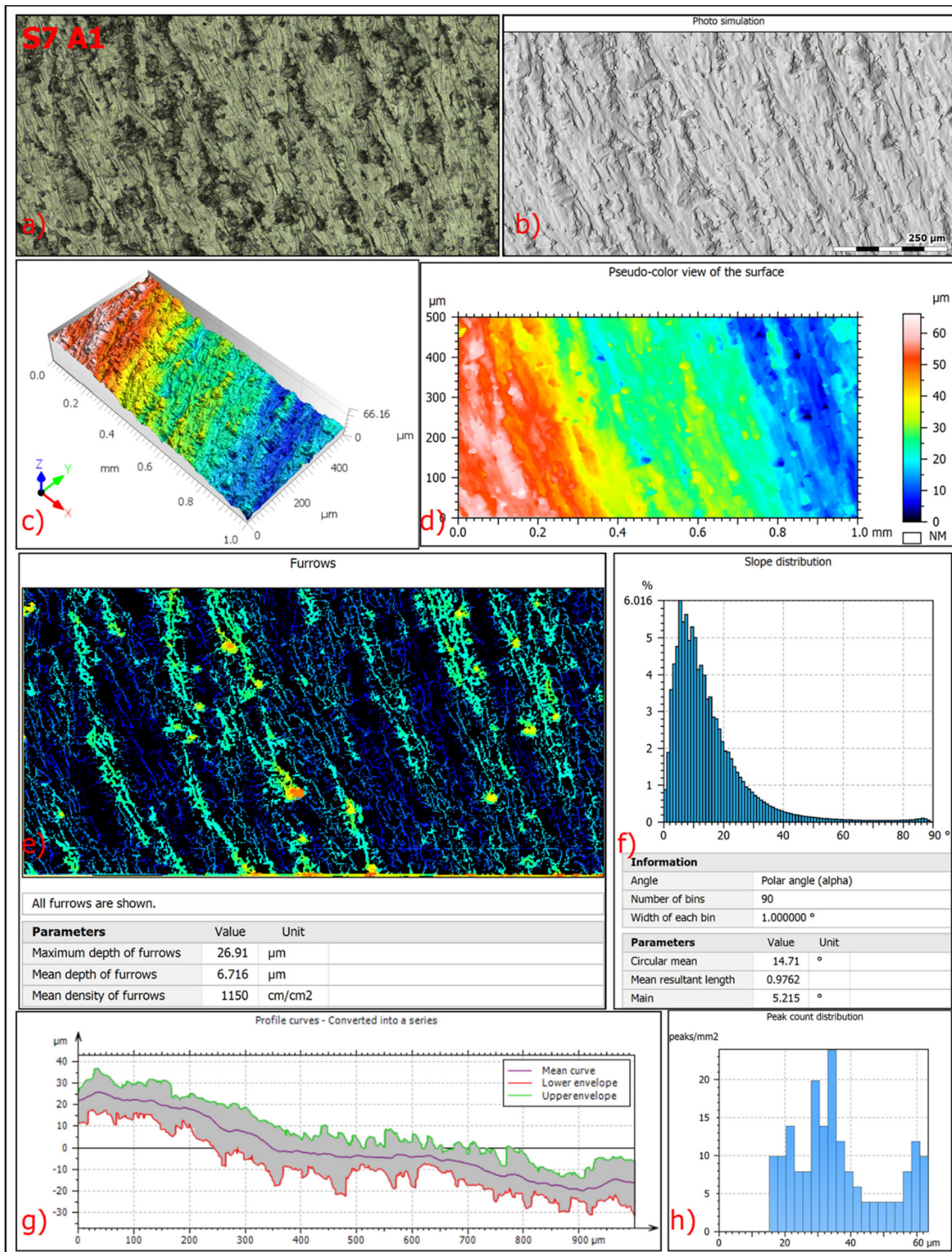
Fig. 10 A1 area of the S7 specimen: **a** texture—true colour view of the image; **b** photo simulation; **c** 3D view of the surface; **d** pseudo-colour view of the surface; **e** furrows; **f** slope distribution; **g** converted into a series—profile curves; **h** peak count distribution histogram
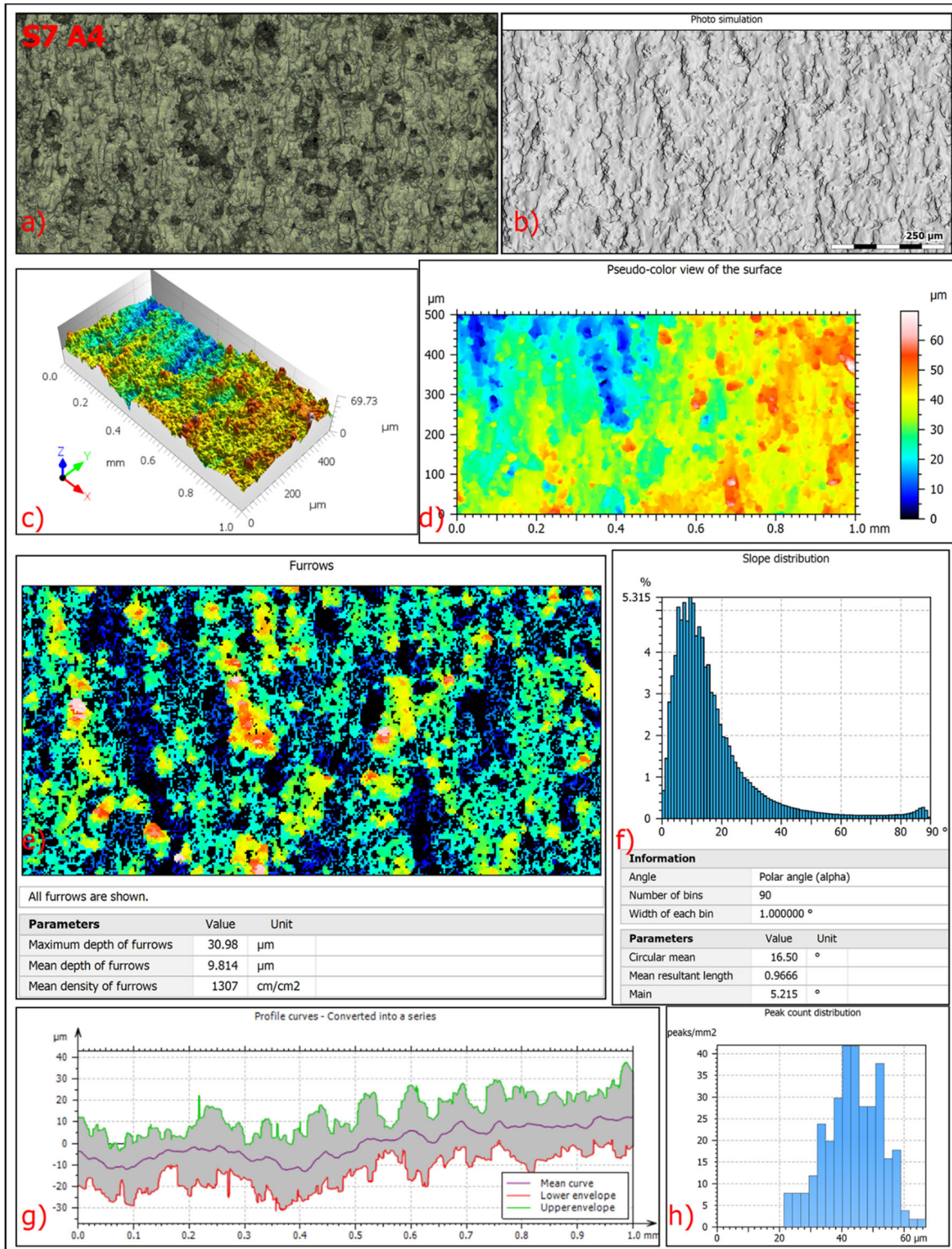
Fig. 11 A4 area of the S7 specimen: **a** texture—true colour view of the image; **b** photo simulation; **c** 3D view of the surface; **d** pseudo-colour view of the surface; **e** furrows; **f** slope distribution; **g** converted into a series—profile curves; **h** peak count distribution histogram
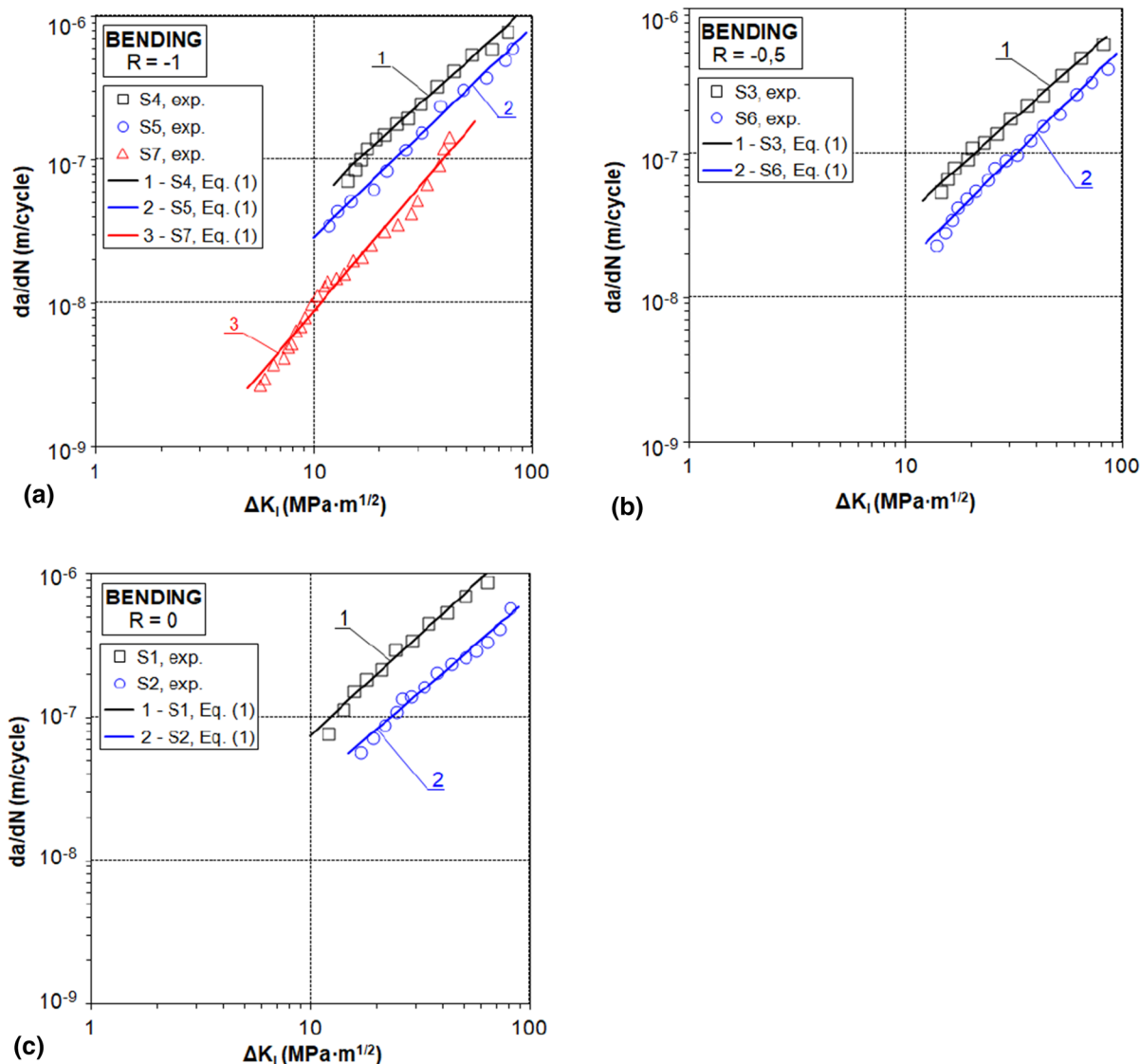
Fig. 12 The results of experimental tests on the fatigue crack growth compared with those calculated according to Eq. (3) for loading ratio: **a** R = − 1 (S4, S5, S7), **b** R = − 0.5 (S3, S6), **c** R = 0 (S1, S2)

Moreover, the change of the stress ratio (e.g. from R = − 1 to R = 0) also causes an increase in the fatigue crack growth rate which can be explained by the mean stress effect. Note that by changing the stress value from σ_{max} = 349 MPa to σ_{max} = 698 MPa (for R = − 1) with a constant value of the SIF range (ΔK_I = 20 MPa·m$^{1/2}$), fatigue crack growth rate increases from da/dN = $3.25 \cdot 10^{-8}$ m/cycle (for σ_{max} = 349 MPa) to da/dN = $1.52 \cdot 10^{-7}$ m/cycle (for σ_{max} = 698 MPa). This represents an increase more than

four-fold. For the loading ratio R = − 0.5 and R = 0 this increase is more than twofold.

The coefficients C and m in formula (3), determined on the basis of experimental tests, were calculated using the least squares method and are presented in Table 5, where the correlation coefficients r are also given at the significance level α = 0.05. The results of bending tests have a relative error not exceeding 20%. In all cases, the correlation coefficients, r, assume values close to 1, which indicates a significant correlation between the results of experimental tests

Table 5 Coefficients C and m of Eq. (3) and correlation coefficients r for the functions shown in Fig. 12

Specimen	Figure	Graph	R	C, m(MPa·m$^{1/2}$)$^{-m}$/cycle	m	r
S4	10a	1	− 1	$2.307 \cdot 10^{-9}$	0.994	0.994
S5	10a	2	− 1	$1.026 \cdot 10^{-9}$	0.994	0.994
S7	10a	3	− 1	$1.467 \cdot 10^{-10}$	0.991	0.991
S3	10b	1	− 0.5	$1.829 \cdot 10^{-9}$	0.996	0.996
S6	10b	2	− 0.5	$5.549 \cdot 10^{-10}$	0.994	0.994
S1	10c	1	0	$2.910 \cdot 10^{-9}$	0.991	0.991
S2	10c	2	0	$1.513 \cdot 10^{-9}$	0.989	0.989
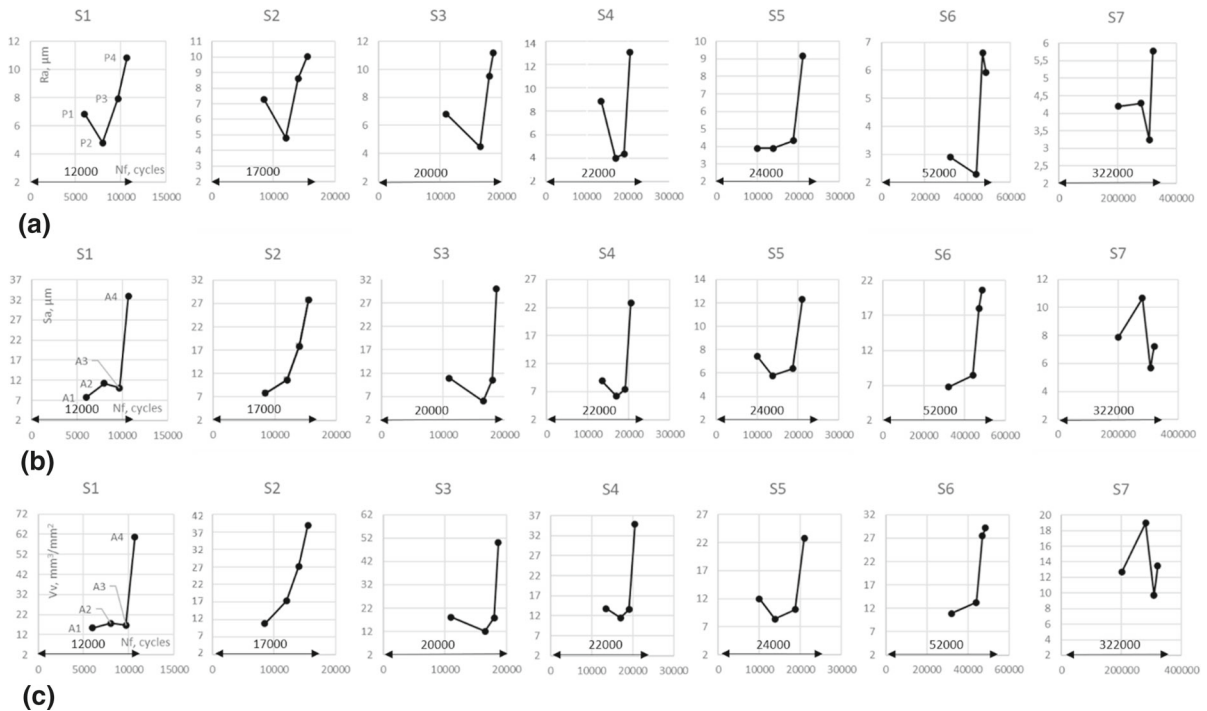
Fig. 13 Values of roughness parameters in number of cycles N context, for four **a** Ra profile parameters; **b** Sa areal parameters; and **c** Vv volume parameters

and those obtained using Eq. (3). Predictably, the values of the C coefficients and m exponents vary with the tested stress ratios R, which proves that the R value has plays an important role on fatigue crack growth behaviour.

For further surface morphology analysis, Ra, Sa and Vv were selected from the parameter groups profile Rx, area Sx and volume Vx, respectively. The measurement results of selected parameters are shown in Fig. 13. The horizontal arrow on the abscissa axes shows the number of cycles to failure Nf, with the actual number indicated above.

In general, roughness can be said to increase along the length of the crack. This trend is clearly observed in Fig. 13a, except for S7 specimen where arithmetical mean height Ra of profile P1 is greater than profile P2. For A1 and A2, arithmetical mean height Sa and void volume Vv (see Fig. 13b, c) have this relationship in only three cases (S3, S4, S5). This is because the roughness in the immediate vicinity of the notch (i.e. at the initiation site) is higher.

The shape of the charts for all parameters (see Fig. 13a, b, c) is clearly different for that of the S7 specimen, which manifests itself in the lowest P3 value for the profile and A3 for the surface.
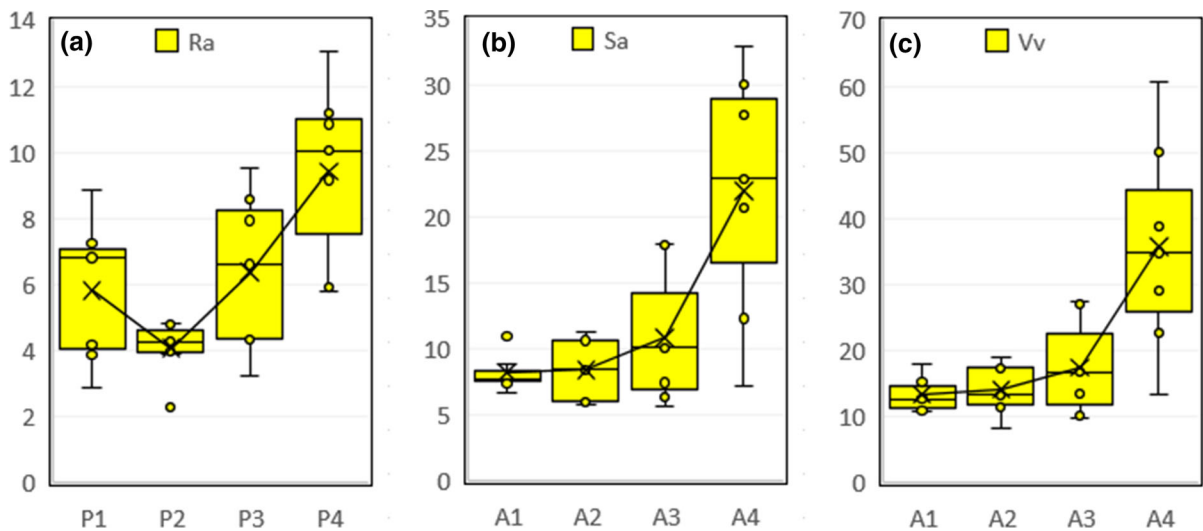
Fig. 14 Average roughness values for individual zones of all fractures: **a** Ra, **b** Sa, **c** Vv
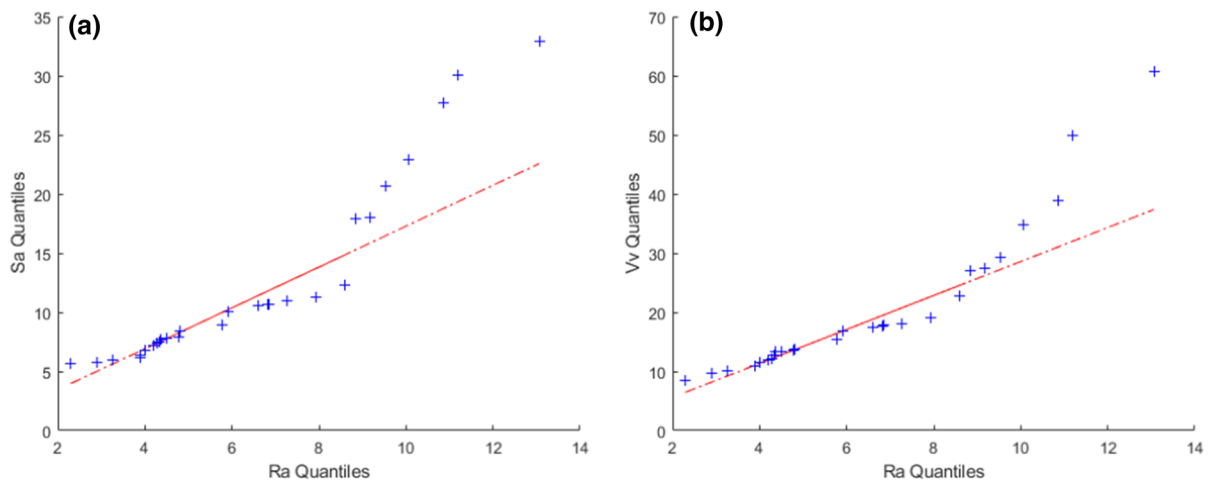

Fig. 15 Quantiles of the data Ra parameter versus the quantiles of data for: **a** Sa parameter; and **b** Vv parameter

Furthermore, Sa and Vv values for the A4 area are not the largest for this case. Compared to the others, the S7 sample has a much higher Nf, which significantly reduces the roughness of the last area.

Samples S6 and S7 for Ra and Sa, Vv, respectively, show the highest values for P3 and A3. These are the samples with the highest fatigue life and with the lowest roughness in terms of the entire fatigue fracture, which clearly agrees with the fact that faster cracking results in greater surface roughness.

Figure 14 presents the average roughness values of all samples for individual zones. As noted in analysis of Fig. 13, roughness in the immediate vicinity of the

notch (i.e. at the crack initiation site) is higher. This fact can be confirmed in Fig. 14a for the Ra values. Averaged Ra value is the smallest for P2, and for P1, P3 and P4 greater percentages about 30.5%, 34.9% and 55.4%, respectively. In contrast, Sa and Vv (see Fig. 14b, c) tend to increase from A1 to A4, and show a very well-defined trend, which is an important outcome.

For all tested specimens (S1–S7), in order to check the correlation between the parameters measured in all areas A1 to A4, with the parameters measured on the profiles P1 to P4, the data are summarized in the Figs. 15 and 16. These are, for Fig. 15, displayed an
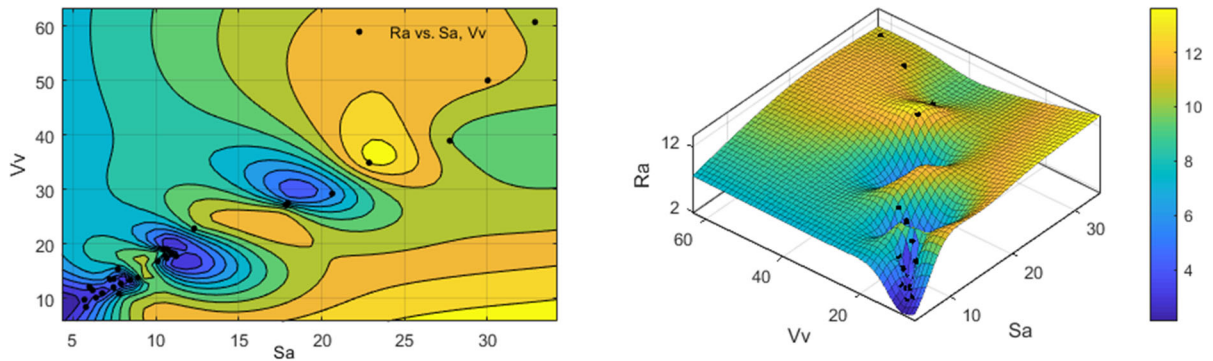
Fig. 16 Interpolation by fitting a surface to the data Ra vs. Sa and Vv parameters

empirical quantile–quantile plot, makes an empirical the quantiles of Ra parameters versus the quantiles of the data in the Sa values (Fig. 15a) and the Vv parameter (Fig. 15b), respectively. These plots produce approximately straight lines suggesting that the two sets of data have the same distribution. On the other hand, Fig. 16 shows the fit surface to all analyzed fracture surface data (Ra, Sa, Vv). A thin-plate spline interpolant approach was used to generate the surface in the plot. Function f(Sa, Vv) is a thin-plate spline computed from coefficient structure, where Sa is normalized by mean (12.36) and standard deviation (7.758), and where Vv is normalized by mean (20.2) and standard deviation (12.63). As can be seen, the fitted function is very well defined for these parameters, with a sum of squared errors (SSE) equal to 7.883×10^{-23}, and a determination coefficient (R^2) equal to 1.

5 Conclusion

In this study, local surface properties of V-notched rectangular cross-section bars made of 2017A-T4 aluminium alloy subjected to bending loading were investigated. The effect of different stress ratios and different stress levels on fatigue crack growth rates and fractography parameters were examined. The following conclusions were drawn:

– Fatigue crack initiation and fatigue crack growth rates were significantly affected by the stress ratio and the stress level. In addition, profile Rx parameters, Sx areal parameters and Vx volume parameters were also affected by the above-mentioned loading variables;

– The analysis conducted using the profiles parameters showed that, in general, there is an increase in the size of peak and valleys with the crack length. Averaged Ra values from all samples showed the following dependencies for the profiles: P1 greater than P2 (30.5%); and P3 and P4 greater than P2 (34.9% and 55.4%, respectively).

– For the analysed fatigue fracture zones (A1 to A4), the arithmetical mean height Sa and void volume Vv evidenced the same relationship than that of the profile parameters (P1 > P2 < P3 < P4) for three cases only. However, the averaged values for Sa and Vv showed a clear trend: A1 < A2 < A3 < A4. This is because Sa and Vv are calculated for extracted areas and volumes, respectively (and not only from profiles collected immediately at the vicinity of the crack initiation site).

– In the crack initiation zone (A1, P1) there are smaller furrows, which is also manifested by a smaller mean angle of slope, than in the final rupture area (A4, P4).

To conclude, it should be highlighted that measurements of fracture surface based on quantitative fractography analyses can contribute to a better understanding of the fatigue failure process. In this paper, the relationship between the fatigue loading parameters and the associated topography parameters is evident for aluminium alloys subjected to cyclic bending. Moreover, the proposed approach grounded on in individual zones of fatigue fractures and the total fracture surface method can capture the effects of stress ratio and stress level.

References

Allum J, Gleadall A, Silberschmidt VV (2020) Fracture of 3D-printed polymers: crucial role of filament-scale geometric features. Eng Fract Mech 224:106818. https://doi.org/10.1016/J.ENGFRACMECH.2019.106818

Aono Y, Noguchi H (2005) Fatigue limit reliability of axisymmetric complex surface. Int J Fract 131:59–78. https://doi.org/10.1007/s10704-004-3638-4

Arakawa K, Takahashi K (1991) Relationships between fracture parameters and fracture surface roughness of brittle polymers. Int J Fract. https://doi.org/10.1007/BF00018393

Berto F, Zappalorto M (2011) Fictitious notch rounding concept applied to V-notches with end holes under mode I loading. Int J Fract 171:91–98. https://doi.org/10.1007/s10704-011-9626-6

Branco R, Prates PA, Costa JD et al (2018) New methodology of fatigue life evaluation for multiaxially loaded notched components based on two uniaxial strain-controlled tests. Int J Fatigue 111:308–320. https://doi.org/10.1016/j.ijfatigue.2018.02.027

Branco R, Costa JD, Berto F et al (2020) Fatigue crack initiation behaviour of notched 34CrNiMo6 steel bars under proportional bending-torsion loading. Int J Fatigue 130:105268. https://doi.org/10.1016/J.IJFATIGUE.2019.105268

Cao Y, Nie W, Yu J, Tanaka K (2014) A novel method for failure analysis based on three-dimensional analysis of fracture surfaces. Eng Fail Anal 44:74–84. https://doi.org/10.1016/J.ENGFAILANAL.2014.04.032

Carpinteri A, Karolczuk A, Macha E, Vantadori S (2002) Expected position of the fatigue fracture plane by using the weighted mean principal Euler angles. Int J Fract 115:87–99. https://doi.org/10.1023/A:1015737800962

Correia JAFO, Huffman PJ, De Jesus AMP et al (2018) Probabilistic fatigue crack initiation and propagation fields using the strain energy density. Strength Mater 50:620–635. https://doi.org/10.1007/s11223-018-0007-5

Faszynka S, Lewandowski J, Rozumek D (2016) Numerical analysis of stress and strain in specimens with rectangular cross-section subjected to torsion and bending with torsion. Acta Mech Autom. https://doi.org/10.1515/ama-2016-0001

He JC, Zhu SP, Liao D et al (2021) Combined TCD and HSV approach for probabilistic assessment of notch fatigue considering size effect. Eng Fail Anal. https://doi.org/10.1016/j.engfailanal.2020.105093

Kahlin M, Ansell H, Basu D et al (2020) Improved fatigue strength of additively manufactured Ti6Al4V by surface post processing. Int J Fatigue 134:105497. https://doi.org/10.1016/J.IJFATIGUE.2020.105497

Kaplonek W, Nadolny K, Królczyk GM (2016) The use of focus-variation microscopy for the assessment of active surfaces of a new generation of coated abrasive tools. Meas Sci Rev 16:42–53

Kobayashi T, Shockey DA (2010) Fracture surface topography analysis (FRASTA)—development, accomplishments, and future applications. Eng Fract Mech 77:2370–2384. https://doi.org/10.1016/J.ENGFRACMECH.2010.05.016

Kowal M, Szala M (2020) Diagnosis of the microstructural and mechanical properties of over century-old steel railway bridge components. Eng Fail Anal. https://doi.org/10.1016/J.ENGFAILANAL.2020.104447

Kulesa A, Kurek A, Łagoda T et al (2016) Comparison of 15Mo3 strain curves obtained for strain-controlled cyclic bending and tension-compression tests. Solid State Phenom 250:85–93

Łagoda T, Macha E, Pawliczek R (2001) Influence of the mean stress on fatigue life of 10HNAP steel under random loading. Int J Fatigue. https://doi.org/10.1016/S0142-1123(00)00108-0

Lauschmann H, Tesař K, Jiroušková K (2019) Quantitative fractography of fatigue cracks: a new solution in 3D. Procedia Struct Integr 23:107–112. https://doi.org/10.1016/J.PROSTR.2020.01.071

Macek W (2019a) Post-failure fracture surface analysis of notched steel specimens after bending-torsion fatigue. Eng Fail Anal. https://doi.org/10.1016/j.engfailanal.2019.07.056

Macek W (2019b) Fractal analysis of the bending-torsion fatigue fracture of aluminium alloy. Eng Fail Anal 99:97–107. https://doi.org/10.1016/j.engfailanal.2019.02.007

Macek W, Łagoda T, Mucha N (2017) Energy-based fatigue failure characteristics of materials under random bending loading in elastic-plastic range. Fatigue Fract Eng Mater Struct. https://doi.org/10.1111/ffe.12677

Macek W, Branco R, Szala M et al (2020a) Profile and areal surface parameters for fatigue fracture characterisation. Materials (basel) 13:3691. https://doi.org/10.3390/ma13173691

Macek W, Branco R, Trembacz J et al (2020b) Effect of multiaxial bending-torsion loading on fracture surface parameters in high-strength steels processed by conventional and additive manufacturing. Eng Fail Anal. https://doi.org/10.1016/j.engfailanal.2020.104784

Macek W, Owsiński R, Trembacz J, Branco R (2020c) Three-dimensional fractographic analysis of total fracture areas in 6082 aluminium alloy specimens under fatigue bending

with controlled damage degree. Mech Mater. https://doi.org/10.1016/j.mechmat.2020.103410

Macek W, Rozumek D, Królczyk GM (2020d) Surface topography analysis based on fatigue fractures obtained with bending of the 2017A–T4 alloy. Meas J Int Meas Confed. https://doi.org/10.1016/j.measurement.2019.107347

Macek W, Marciniak Z, Branco R et al (2021) A fractographic study exploring the fracture surface topography of S355J2 steel after pseudo-random bending-torsion fatigue tests. Measurement. https://doi.org/10.1016/j.measurement.2021.109443

Martelo D, Sampath D, Monici A et al (2019) Correlative analysis of digital imaging, acoustic emission, and fracture surface topography on hydrogen assisted cracking in Ni-alloy 625+. Eng Fract Mech 221:106678. https://doi.org/10.1016/J.ENGFRACMECH.2019.106678

Martins RF, Branco R, Long X (2020) Fatigue life assessment in bainitic steels based on the cumulative strain energy density. Appl Sci 10:7774. https://doi.org/10.3390/app10217774

McDowell DL (1989) Basic issues in the mechanics of high cycle metal fatigue. Int J Fract 80:103–145. https://doi.org/10.1007/BF00012666

Mendes P, Correia JAFO, De Jesus AMP et al (2020) A brief review of fatigue design criteria on offshore wind turbine support structures. Frat Ed Integrità Strutt Ed Integrità Strutt 15:302–315. https://doi.org/10.3221/igf-esis.55.23

Moreira MF, Fantin LB, Beneduce Neto F, Azevedo CRF (2020) Microstructural and mechanical characterization of as-cast nickel-based superalloy (IN-713C). Int J Met. https://doi.org/10.1007/s40962-020-00540-0

Owsiński R, Niesłony A (2016) Analytical model of dynamic behaviour of fatigue test stand—description and experimental validation. In: Springer Proceedings in Mathematics and Statistics

Paris P, Erdogan F (1963) A critical analysis of crack propagation laws. J Fluids Eng Trans ASME 85:528–533. https://doi.org/10.1115/1.3656900

Pickard AC (1986) The application of 3-dimensional finite element methods to fracture mechanics and fatigue life prediction. Chameleon Press LTD, London

Rozumek D, Faszynka S (2016) Fatigue crack growth in specimens with rectangular section under torsion and bending with torsion. Solid State Phenom 250:10–15

Rozumek D, Faszynka S (2017) Influence of the notch radius on fatigue crack propagation in beam specimens of 2017A–T4 alloy. Mater Sci. https://doi.org/10.1007/s11003-017-0090-y

Rozumek D, Faszynka S (2020) Surface cracks growth in aluminum alloy AW-2017A-T4 under combined loadings. Eng Fract Mech 226:106896. https://doi.org/10.1016/J.ENGFRACMECH.2020.106896

Skibicki D, Pejkowski Ł (2017) Low-cycle multiaxial fatigue behaviour and fatigue life prediction for CuZn37 brass using the stress-strain models. Int J Fatigue. https://doi.org/10.1016/j.ijfatigue.2017.04.011

Slámečka K, Pokluda J, Kianicová M et al (2010) Quantitative fractography of fish-eye crack formation under bending-torsion fatigue. Int J Fatigue. https://doi.org/10.1016/j.ijfatigue.2009.07.009

Świrad S, Wydrzynski D, Nieslony P, Krolczyk GM (2019) Influence of hydrostatic burnishing strategy on the surface topography of martensitic steel. Measurement 138:590–601. https://doi.org/10.1016/J.MEASUREMENT.2019.02.081

Wang Y, Meletis EI, Huang H (2013) Quantitative study of surface roughness evolution during low-cycle fatigue of 316L stainless steel using Scanning Whitelight Interferometric (SWLI) Microscopy. Int J Fatigue. https://doi.org/10.1016/j.ijfatigue.2012.11.009

Wu D, Yao C, Zhang D (2018) Surface characterization and fatigue evaluation in GH4169 superalloy: comparing results after finish turning; shot peening and surface polishing treatments. Int J Fatigue. https://doi.org/10.1016/j.ijfatigue.2018.04.009

Zeravcic VS, Djukic M, Bakic G, et al (2006) Case study of supporting tubes failure. In: Fracture of Nano and Engineering Materials and Structures—Proceedings of the 16th European Conference of Fracture. Kluwer Academic Publishers, pp 1081–1082

Zhang H, Fatemi A (2010) Short fatigue crack growth behavior under mixed-mode loading. Int J Fract 165:1–19. https://doi.org/10.1007/s10704-010-9497-2